

Graphene Tunable Plasmon–Phonon Coupling in Mid-IR Complementary Metamaterial

Nan Chen, Dihan Hasan, Chong Pei Ho, and Chengkuo Lee*

Metamaterial-based plasmonics has become an overwhelming research field due to its enormous potential and versatility in molecular sensing, imaging, and nonlinear optics. This work presents a new tunable plasmonic platform on which the metamaterial resonance is coupled with infrared vibrational bond in the presence of graphene electrostatic modulation. The maximum electric field enhancement factor induced by mode coupling is 14 and the quality factor (Q-factor) of phonon mode is increased approximately by fourfold. The graphene electrostatic modulation based on the parallel-plate capacitor configuration enables a wavelength shift of 1.57 nm V^{-1} , resonance intensity and Q-factor modulation depth of 103.34% and 70%, respectively. Metamaterial based plasmon polariton perfectly matched with phonon mode yields the highest Q-factor of 40. However, this perfectly matched resonance appears to be prohibitively “switched off” in the electrostatic tuning, which is reported for the first time. Mode splitting investigation reveals the largest coupling strength of 8.1 meV (1.96 THz) that results in the insensitivity to the perturbation caused by graphene modulation. Finally, an averaged sensitivity of $1.677 \mu\text{m RIU}^{-1}$ and a tunable figure of merit are reported, depicting the versatility of this platform for multiplexed sensing applications in various conditions.

1. Introduction

The vibrational fingerprints of molecular compounds are abundant at mid-infrared. The technique of infrared spectroscopy enables a wide range of sensing applications from molecular identification to hazardous gas detection and

concentration monitoring.^[1] In order to improve sensing accuracy, the engineered photon-electron oscillation resonant along the interface or confined in the subwavelength metamaterial can be utilized.^[2] This collective electromagnetic oscillating behavior known as plasmonic resonance is able to express the unique optical features under different conditions. Among the various types of plasmonic resonances, Fano resonance is characterized by the sharp asymmetric line shape, created by the interference of a narrow discrete state (black or sub-radiant mode) with the broadband continuum state (bright or super-radiant mode) and is favorable for constructing slow light or nonlinear optical platform to launch the high-Q enhanced applications, such as biochemical sensing.^[3–6] The most popular approach to the excitation of Fano resonance in the mid-infrared frequency range is to break the symmetry of metamaterial geometry.^[7–9] There

are other methods including the multistacking of thin metal and dielectric layers^[10] and making use of material intrinsic damping as the subradiant mode.^[11–13] For example, with the mid-infrared vibrational absorption resonance (phonon band) of silicon dioxide as the dark mode, the strong Fano coupling between the SiO₂ thin film and metamaterial split ring resonator (SRR) is observed such that it leads to mode splitting featured as frequency anticrossing.^[13] In the asymmetric SRR metamaterial, polymethyl-methacrylate (PMMA) produced Fano resonance is enhanced as well.^[14] The Fano resonance from metamaterial plasmon coupled with the phonon vibration of PMMA is varied through changing metamaterial geometry.^[11,15] Moreover, the realization of the ultrasensitive detection of polymer molecule is obtained through matching the polymer phonon resonance with the Fano resonance of periodic nanostructures.^[16] The alteration of Fano resonance can be achieved by the individual or simultaneous control of dark and bright resonance. The aforementioned geometry variation of subwavelength metamaterial can be used to shift the broad bright mode resonance. The alternative approaches such as mechanical stress,^[17] liquid crystal,^[18] micro electromechanical system technology^[19] are exploited to either modify the optical properties of the surrounding material or actively reconfigure the structure. Recently, the dynamic manipulation of Fano resonance by graphene electrostatic tuning has been demonstrated by some groups.^[20,21]

N. Chen, Dr. D. Hasan, Dr. C. P. Ho, Prof. C. Lee
Department of Electrical & Computer Engineering
National University of Singapore
4 Engineering Drive 3, 117583, Singapore
E-mail: elelc@nus.edu.sg

N. Chen, Dr. D. Hasan, Prof. C. Lee
Center for Intelligent Sensors and MEMS
National University of Singapore
E6 #05-11F, 5 Engineering Drive 1, Singapore 117608, Singapore

N. Chen, Dr. D. Hasan, Prof. C. Lee
NUS Suzhou Research Institute (NUSRI)
Suzhou Industrial Park
Suzhou 215123, P. R. China

Prof. C. Lee
Graduate School for Integrative Science and Engineering
National University of Singapore
117456, Singapore

 The ORCID identification number(s) for the author(s) of this article can be found under <https://doi.org/10.1002/admt.201800014>.

DOI: 10.1002/admt.201800014

Monolayer graphene has been explored to enrich the mid-infrared plasmonic sensing performance due to the remarkable flexibility and feasibility offered by the unique monoatom structure.^[22,23] The significance of monolayer graphene also refers to the sensitivity in detection and the controllability by the means of electrostatic doping, chemical doping, thermoelectric, magnetic, optical mechanism, etc.^[24–30] For instance, graphene plasmon enhanced vibrational carbonyl resonance in PMMA thin film is experimentally revealed.^[31] Combined with spectroscopy technology, the tunable graphene plasmon at mid-infrared is successfully demonstrated for the advanced detection of protein amide I and II and monolayer graphene manifests its advantage over the noble metals with respect to the superior spatial light confinement.^[1] Additionally, monolayer graphene has been widely used as the tunable medium: changing metamaterial-based resonance damping is realized with the aid of graphene electrical modulation^[32]; extraordinary optical transmission of the metallic complementary metamaterial is electrically controlled by the patterned graphene ribbon^[33]; Fano resonance originated from the designed nanostructure is able to be manipulated by the electrostatic tuning of graphene with the silicon back-gating and ion-liquid gating configuration,^[34] as well as by electrical switching in the source–drain configuration.^[9]

When it comes to engineering the metamaterial-based plasmon resonance, one way is to manipulate the geometric dimension of unit cell. The other way is to utilize the tunability of graphene. Both methods are employed in this work so that (a) the coupling of phonon mode with metamaterial induced plasmon resonance and (b) this coupling modulated by graphene can be insightfully observed. Besides, the metamaterial plasmonic resonance is engineered to align with the intrinsic vibrational carbonyl bond of PMMA for Fano-like line shape at mid-infrared. With further improvement of graphene electrical tuning made based on Wan et al.'s work,^[11] the progressive tuning effect on the coupled resonance could be obtained. During graphene electrostatic modulation, the perfectly matched plasmon–phonon resonance is surprisingly resistant to change. To the best of our knowledge, such plasmon–phonon coupling behavior enabled by graphene modulation is first observed to date. Meanwhile, the theoretical explanation made by mode splitting and coupling strength, fills the gap that most of the vacuum Rabi splitting from nanocluster, nanoaggregate, or plexiton are discussed in visible light.^[35–39] Although there are some works applying mode splitting theory for mid-infrared exploration,^[2,11,13,40] no study of the tunable behavior in the presence of graphene has been made yet. Therefore, our work reports the mode splitting analysis of graphene tuning coupled resonance in mid-infrared region for the first time. This is a newly applied approach to investigate how the graphene electrical modulation could control the coupled resonance, such as by coupling strength. Incorporating graphene as an active medium will also cater the need for dynamic reconfiguration for performing multiplexed sensing in various conditions on the single platform.

The overall organization of the paper is as follows. The first section will introduce the metamaterial enhanced high-Q Fano-like resonance. Next, monolayer graphene's electrostatic modulation of the plasmonic resonator will be shown and the spectral change will be discussed. Afterward, the numerical analysis

using three-level model is presented with the extracted parameters of resonance coupling. The subsequent section mainly concentrates on the coupling process in terms of mode splitting and coupling strength. Last but not least, the potential application of molecule sensing on the proposed platform is discussed and demonstrated. The new feature realized by graphene tuning can be viable to achieve better sensing performance.

2. Results and Discussion

2.1. Mid-Infrared Responses of High-Q Fano Resonance

This paper presents three cross-shaped metamaterial designs, each of which is comprised of 30×30 unit cell array with 2.5 μm periodicity. They are distinguished from one another in different lengths: 1.9 μm, 2.1 μm, and 2.3 μm as shown in **Figure 1d–f**, while the width is fixed at 100 nm. In a two-step state-of-the-art fabrication, beginning with single layer graphene substrate and coating with PMMA resist, the device was written by electron beam lithography and then developed to obtain the periodic subwavelength structures, followed up with gold deposition shown in **Figure 1a–c**. **Figure S1a–c** (Supporting Information) clarifies that the gold layer is formed along the developed PMMA void gap and attached with the bottom graphene layer. This metal layer, on one hand, is served as the plasmonic platform to enhance surface localized plasmon polariton confinement. On the other hand, it is the terminal for electrostatically doping the sandwiched monolayer graphene in the parallel-plate-capacitor configuration, while the doped silicon substrate connected to ground is the other terminal. The conceptual schematic measurement setup is shown in **Figure 1g**. Adjusting the applied terminal bias to actively control the Fermi level of the monolayer graphene is able to alter the spectral location of the localized surface plasmon resonance (LSPR).

PMMA, a widely used photoresist in micro/nanofabrication, has strong asymmetric fingerprint of carbonyl stretching bond vibration at 5.77 μm.^[16] In **Figure 1h**, the spectra of the device before and after metal deposition are compared to give a profound insight that this carbonyl mode can be greatly enhanced by LSPR mode and its Q-factor substantially increases from 5.01 to 21.74. Furthermore, as shown in **Figure 1i** of the simulated electric field enhancement distribution of 0° polarization at 5.77 μm, the maximum enhancement factor $\frac{|E_2|^2}{|E_1|^2}$ is 14.02

residing along the cross slot. LSPR's coupling with phonon resonance has strengthened electromagnetic field confinement with plasmon polariton modifying the near-field permittivity.

In order to realize the maximum plasmon–phonon enhancement, the carbonyl vibration band is expected to overlap the LSPR mode. Here we vary the length of the metamaterial cross pattern and investigate the following dimensions in the finite-difference time-domain (FDTD) simulation (**Figure 2a**): 1.9 μm (device A), 2.1 μm (device B), and 2.3 μm (device C) in length; 100 nm in all widths. The LSPR wavelength is proportional to the length of cross pattern because shorter “dipolar” effective length excites resonance at higher frequency (see Section 3, Supporting Information). The simulated magnetic field distributions of device C at 6.40 μm and 2.48 μm under 0°

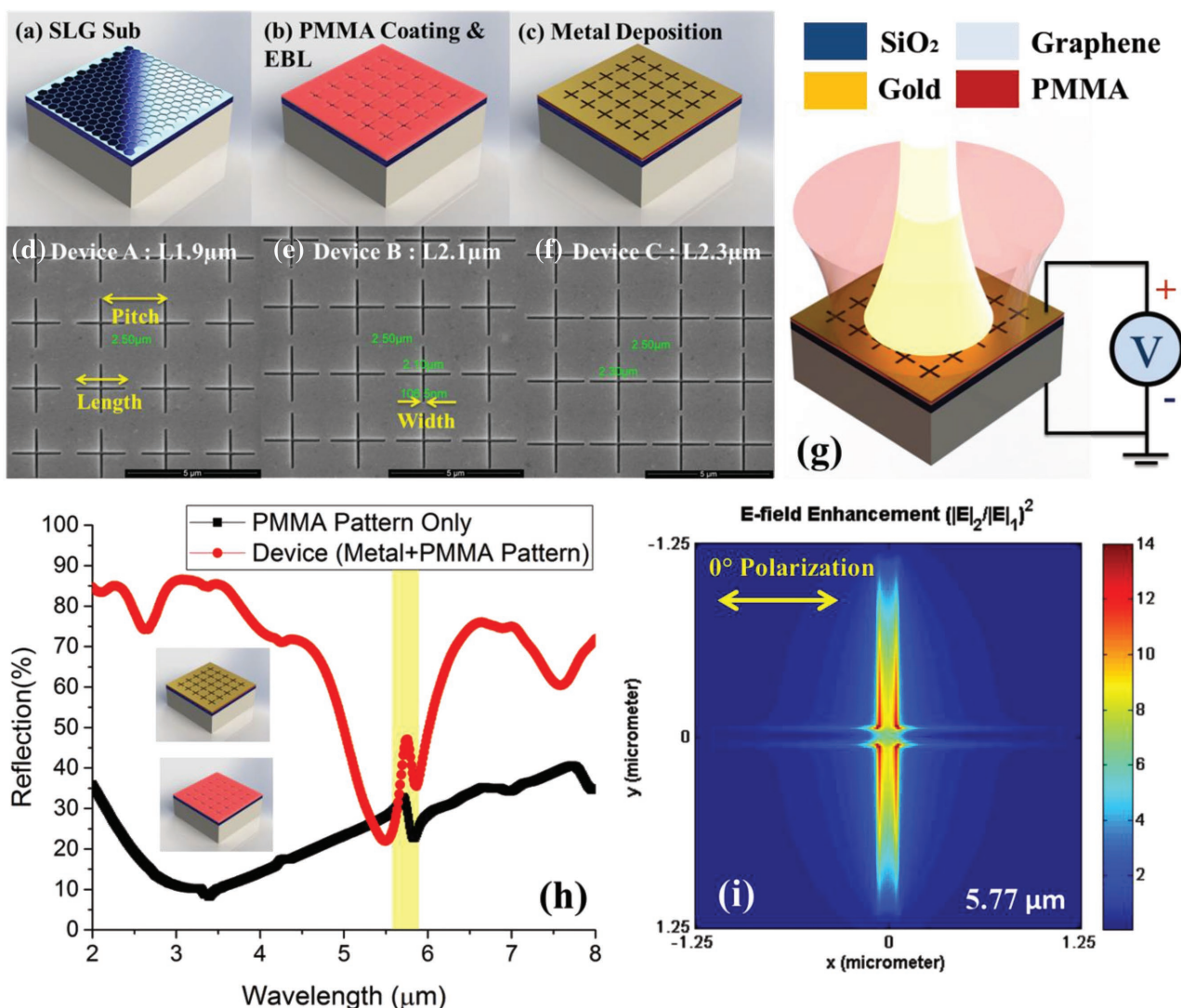


Figure 1. a–c) The schematics of device in fabrication progress; d–f) SEM photos of device A, B, and C; g) The schematic of device under electrical tuning with incident light; h) The measured reflection spectra of device without and with top metal layer; i) The electric field enhancement of device with metal versus nonmetal at 5.77 μm at 0° polarization.

polarization are depicted in Figure 2b,c from which the strong “dipole” mode and weak “quadruple” mode can be clearly identified and notably these two LSPRs are along 90° polarization, consistent with the Babinet’s principle.^[41,42]

The material models in FDTD are: Falkovsky model (mid-infrared) for monolayer graphene with the effective thickness of 1 nm, Palik model for gold, silicon dioxide, and silicon substrate. For the optical property of PMMA at mid-infrared, the Lorentz oscillator model is applied as^[14]

$$\epsilon_{PMMA} = \epsilon_0 + \epsilon_L \omega_0^2 / (\omega_0^2 - 2i\delta_0 \omega - \omega^2) \quad (1)$$

where the relative permittivity of PMMA ϵ_0 is 2.2, the oscillator strength ϵ_L is 0.04, the Lorentz resonance frequency ω_0 is $3.269 \times 10^{14} \text{ rad s}^{-1}$ (5.77 μm or 52 THz), and the damping rate δ_0 is chosen as $2.8 \times 10^{12} \text{ rad s}^{-1}$ (0.446 THz) to match with the experiment results. The impact of different line widths on the

overall resonance spectrum refers to Figure S2 (Supporting Information).

Figure 2d,e is the measured spectra of fresh and post-thermal-treated device after bonding. The accumulated thermal effect in the bonding process leads the undesired residual stress to the structure and changes material property to some extent,^[43] so the spectral shift and shrink are observed other than severe distortion at 6.5–7 μm (in the Supporting Information). However, device B exhibits the matched plasmon–phonon coupling which is aligned with simulation. Q-factors of Fano-like peaks are 22.32, 40.19, and 7.12 for postdevice A, B, and C, respectively. Thus, tailoring LSPR to be spectrally overlapped with the carbonyl mode can successfully launch the high-Q Fano resonance. Figure S3b,d,f (Supporting Information) of the simulated E-field distributions at the Fano-like peak frequencies of three devices reveal the maximum magnitude of $|E|^2$

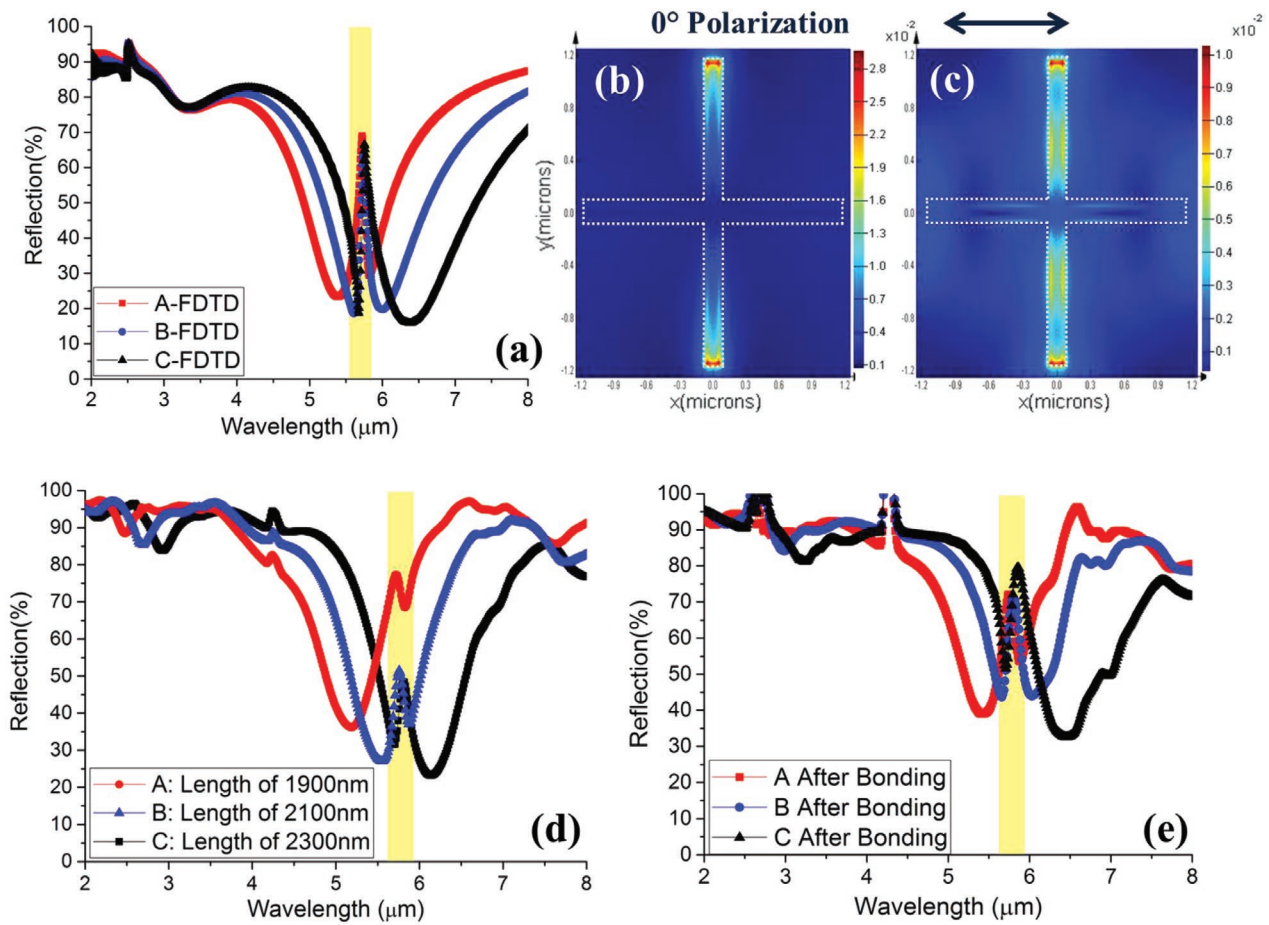


Figure 2. a) The simulated reflection spectra of device A, B and C. The highlighted yellow band indicates the location of PMMA carbonyl resonance band; b) The simulated magnetic field distribution of LSPR “dipole” mode at 6.40 μm of device C; c) The simulated magnetic field distribution of LSPR “quadrupole” mode at 2.48 μm of device C; d) The measured reflection spectra of device A, B, and C before bonding; e) The measured reflection spectra of postthermal-treated device A, B, and C after bonding.

spatially localized over the narrow slot in the following order: Device B > Device A > Device C, in agreement with the respective Q-factors. The next section will focus on manipulating the optical response by graphene electrostatic tuning.

2.2. Electrostatic Modulation of Monolayer Graphene on the Plasmonic Resonator

The free carrier concentration of monolayer graphene can be easily modulated by applying external bias, so is Fermi level related to surface conductivity. The relationship of surface conductivity of monolayer graphene σ_g from both intraband and interband transitions and Fermi level E_F is expressed as following (including spin effect)

$$\sigma_g(\omega) = \sigma_{\text{intra}}(\omega) + \sigma_{\text{inter}}(\omega) = \frac{2ie^2k_B T}{\pi\hbar^2(\omega + i/\tau)} \ln \left[2 \cosh \left(\frac{E_F}{2k_B T} \right) \right] + \frac{e^2}{4\hbar} \left[\frac{1}{2} + \frac{1}{\pi} \arctan \left(\frac{\hbar\omega - 2E_F}{2k_B T} \right) - \frac{i}{2\pi} \ln \left(\frac{(\hbar\omega + 2E_F)^2}{(\hbar\omega - 2E_F)^2 + (2k_B T)^2} \right) \right] \quad (2)$$

where e is the electric charge, \hbar is the reduced Planck constant, k_B is the Boltzmann constant, T is the temperature, and ω is

the frequency of incident light. The carrier relaxation time is $\tau = \mu E_F / e v_F^2$, and μ is the carrier mobility. At mid-infrared frequencies, the contribution from interband transition is negligible. For simplicity, the conductivity of graphene at mid-infrared is approximated to $\sigma_{\text{intra}}(\omega) = \frac{2ie^2k_B T}{\pi\hbar^2(\omega + i/\tau)} \ln \left[2 \cosh \left(\frac{E_F}{2k_B T} \right) \right]$. The permittivity of graphene ϵ_g governed by optical conductivity σ_g can be written as below^[25,44]

$$\epsilon_g(\omega) = 1 + \frac{i\sigma_{\text{intra}}(\omega)}{\omega\epsilon_0 t_g} \quad (3)$$

where ϵ_0 is the permittivity of vacuum. t_g is the thickness of monolayer graphene. Consequently, the permittivity of monolayer graphene is electrically controllable by Fermi level linked to the total carrier density N in Equation (4)

$$E_F = \hbar v_F \sqrt{\pi N} \quad (4)$$

where v_F is the Fermi velocity and commonly taken as $1 \times 10^6 \text{ m s}^{-1}$. In the parallel-plate capacitor configuration, the total carrier density can be quantified by the applied V_{bias} as in $N = C_g |V_{\text{bias}} - V_{\text{CNP}}| / e = \epsilon_0 \epsilon_r |V_{\text{bias}} - V_{\text{CNP}}| / e t_d$ where C_g is the gate capacitance per unit area and ϵ_r is the relative

Table 1. Calculated Fermi level at different applied bias.

| Applied bias | 20 V | 40 V | 60 V | 80 V | 100 V | 120 V | 140 V | 160 V | 180 V |
|------------------|-------|-------|-------|-------|-------|-------|-------|-------|-------|
| Fermi level [eV] | 0.071 | 0.100 | 0.123 | 0.142 | 0.158 | 0.174 | 0.187 | 0.200 | 0.213 |

permittivity of silicon oxide.^[45] The thickness of silicon oxide dielectric isolation layer t_d is 300 nm. Then the correlation between the applied bias and the Fermi level of monolayer graphene can be expressed as

$$E_F = \hbar v_F \cdot \sqrt{\frac{\pi \epsilon_0 \epsilon_r |V_{\text{bias}} - V_{\text{CNP}}|}{et_d}} = 0.0158 \times \sqrt{|V_{\text{bias}} - V_{\text{CNP}}|} \quad (5)$$

V_{CNP} is the charge neutral point (CNP) also known as the Dirac point of the E - k dispersion of monolayer graphene. At this point there is no energy state in between thus envisioning the lowest electrical conductance. The pure monolayer graphene has a positive CNP because of the p -doped silicon substrate. But the additional electrons imposed by PMMA, metal layer, and thermal annealing can possibly balance the original CNP. Assuming V_{CNP} equal to 0 V, the calculated values of Fermi level corresponding to different applied bias are listed in **Table 1**. To theoretically verify the trend of the observed spectral shift, the Fermi levels of monolayer graphene model are set from 0.1 to 0.25 eV, in step of 0.05 eV in FDTD simulation. The permittivity of graphene FDTD model at various Fermi levels can be found in Figure S4 (Supporting Information). The real part of graphene permittivity is decreased at high doping concentrations.

The measured and simulated spectra of the three devices modulated by different graphene doping concentrations are shown in **Figure 3**. The insets provide the close-up view of the tuning trend of LSPR dip or the fixed Fano-like peak and the arrows indicate the direction of tuning.

As seen in Figure 3a,e, there is blueshift in LSPR wavelength and increase in the reflection intensity of LSPR dip as the applied bias ranging from 0 to 180 V for device A and C. However, such trend is hardly observed for device B in Figure 3c. The electrostatic modulation barely takes effect in the Fano-like peak generated from the perfectly matched plasmon–phonon resonance in device B: tunability being “shut off” under the exact same electrostatic tuning condition of graphene as device A and C. Overall, the trend of experiment data is observed in good consent with the corresponding simulation results.

To have a straightforward understanding of graphene’s electrical tuning effect, the LSPR wavelength and intensity as a function of applied bias are plotted in **Figure 4a,b** for device A and C. With the applied bias varying from 0 to 180 V, the resonance wavelength of device A experiences blueshift from 5.4232 μm to 5.3850 μm , by 38.2 nm; resonance intensity is increased from 38.95% to 53.58%, by 37.56%. Device C also undergoes the blueshift from 6.4586 μm to 6.2993 μm by 159.3 nm; the reflection intensity is increased from 32.61% to 66.31% by 103.34%. Monolayer graphene with higher carrier density being more metallic enables blueshift of LSPR wavelength as well as higher reflection intensity. Figure 4c depicts the blueshift of LSPR wavelength of device A and C with the reference point of 0 V. Device A has the complete linear modulation range with

the sensitivity of 0.21 nm V^{-1} , while the linear region of device C is 40–120 V with much higher sensitivity of 1.57 nm V^{-1} and saturated at high voltages of 140–180 V. The fitted equations of device A and C are available in the Supporting Information.

Aside from wavelength shift and intensity change of LSPR, resonance’s Q-factors of device A and C also deliver the tunability in Figure 4d (refer to Table S1 for specific values, Supporting Information). The Q-factors of Fano-like peak of device A and C are ascended and descended by 70.12% and 52.13%, respectively, while the LSPR Q-factors for device A and C are declined and elevated throughout the entire tuning process. As discussed, graphene electrical modulation is not significantly applicable to device B, which will be further analyzed by the coupled level model and mode splitting theory in the following sections.

2.3. Numerical Investigation of Plasmon–Phonon Coupling by Graphene Modulation

The three-level model in quantum optics is able to provide an account for the resonance stemmed from photon–phonon–electron coupling by modeling the motion of density matrix elements.^[46–49] The existence of ground state $|0\rangle$, excited state $|1\rangle$, and metastable state $|2\rangle$ allows three level transition, akin to two driven coupled harmonic oscillator.^[6,31,50–52] The possible energy level transition paths are: (1) $|0\rangle - |1\rangle$ bright mode of LSPR excitation and (2) $|0\rangle - |1\rangle - |2\rangle - |1\rangle$ dark mode of phonon resonance coupled with LSPR, whereas $|0\rangle - |2\rangle$ route is strictly forbidden. The coupling process can be described as

$$\begin{aligned} \dot{\tilde{\rho}}_{10} &= i(\omega - \omega'_{\text{LSPR}} + i\gamma'_{\text{LSPR}})\tilde{\rho}_{10} + \frac{i\Omega_P}{2} + \frac{i\tilde{\rho}_{20}\Omega_C}{2} \\ \dot{\tilde{\rho}}_{20} &= i(\omega - \omega'_{\text{LSPR}} - \delta + i\gamma_{\text{PMMA}})\tilde{\rho}_{20} + \frac{i\tilde{\rho}_{10}\Omega_C^*}{2} \end{aligned} \quad (6)$$

Where $\tilde{\rho}_{10} = \rho_{10} e^{i\omega t}$ and $\tilde{\rho}_{20} = \rho_{20} e^{i(\omega - \omega_c)t}$ are the density matrix elements of bright and dark modes. $\Omega_P(\omega)$ and $\Omega_C(\omega_c)$ represent the power of the pumping and coupling lights. γ_{LSPR} and γ_{PMMA} are denoted as the damping rate of bright and dark resonance, equal to the corresponding full width at half maximum (FWHM). ω is angular frequency of the incident field and ω'_{LSPR} is the frequency of bright mode. ω_{PMMA} and γ_{PMMA} are 52 and 0.446 THz, respectively. $\delta = \omega_c - \omega_{12}$ is the detuning of dark and bright excitations that quantifies the resonance asymmetry. Detuning δ being away from zero diverts the symmetric Lorentzian lineshape from the asymmetric Fano lineshape. In adiabatic regime when $\dot{\tilde{\rho}}_{10}$ and $\dot{\tilde{\rho}}_{20}$ are both zero, $\tilde{\rho}_{10}$ can be obtained as

$$\tilde{\rho}_{10} = \frac{\frac{\Omega_P}{2}(\omega - \omega'_{\text{LSPR}} - \delta + i\gamma_{\text{PMMA}})}{\frac{\Omega_C^2}{4} - (\omega - \omega'_{\text{LSPR}} + i\gamma'_{\text{LSPR}})(\omega - \omega'_{\text{LSPR}} - \delta + i\gamma_{\text{PMMA}})} \quad (7)$$

The reflection spectrum of the proposed device can be obtained by $\text{Im}(-\tilde{\rho}_{10})$ which portrays energy dissipation. Through equation fitting, the related parameters (i.e., coupling coefficients, detuning factors, damping rates, resonance frequencies) are extracted in Tables S2–S4 (Supporting

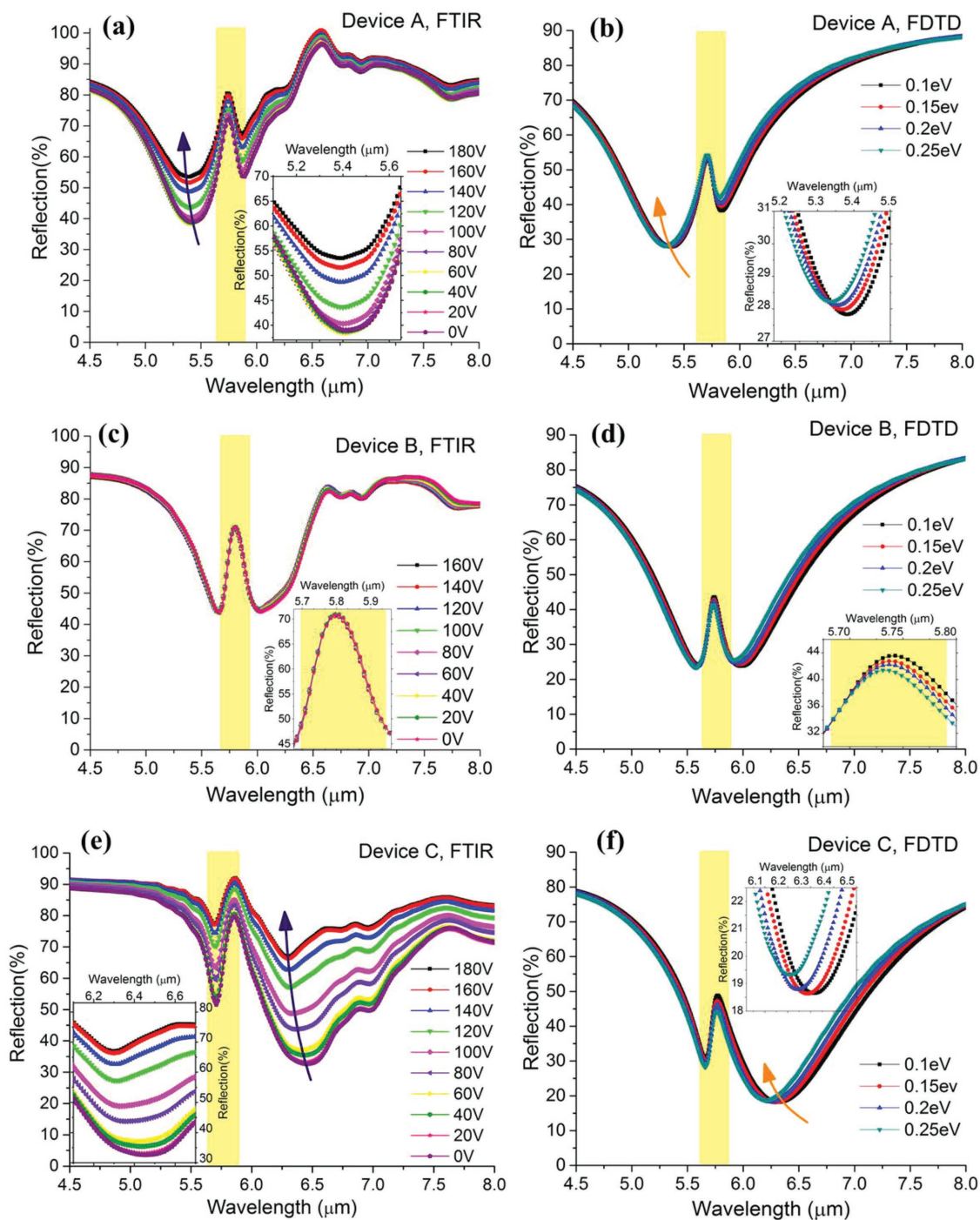


Figure 3. a,c,e) The measured reflection spectra at different applied voltages from 0 to 180 V of device A, B, and C; b,d,f) The simulated reflection spectra at different Fermi levels from 0.1 to 0.25 eV of device A, B, and C.

Information) and displayed in **Figure 5**. Figure S7a,c,e shows the comparison of the measurement spectrum with the fitted curve of device A, B, and C at the applied bias of 0 V. The errors in the fitted values of device C are estimated to be 0.15–1.1 THz which are higher than the previous fittings of device A and B. Figure S7b,d,f (Supporting Information) displays the fitted curves from 0 to 180 V of all three devices.

From the fitted results, one clear observation is that the detuning δ of device A and C has the opposite sign which is congruous with the asymmetric Fano line shape. Besides, the detuning of device A is proportional to the increased graphene doping level, whereas device C is inversely proportional to that, which exerts that asymmetry of Fano line shape can be tuned by graphene modulation. The detuning of device B is close to zero so its peak can be treated as the moderate

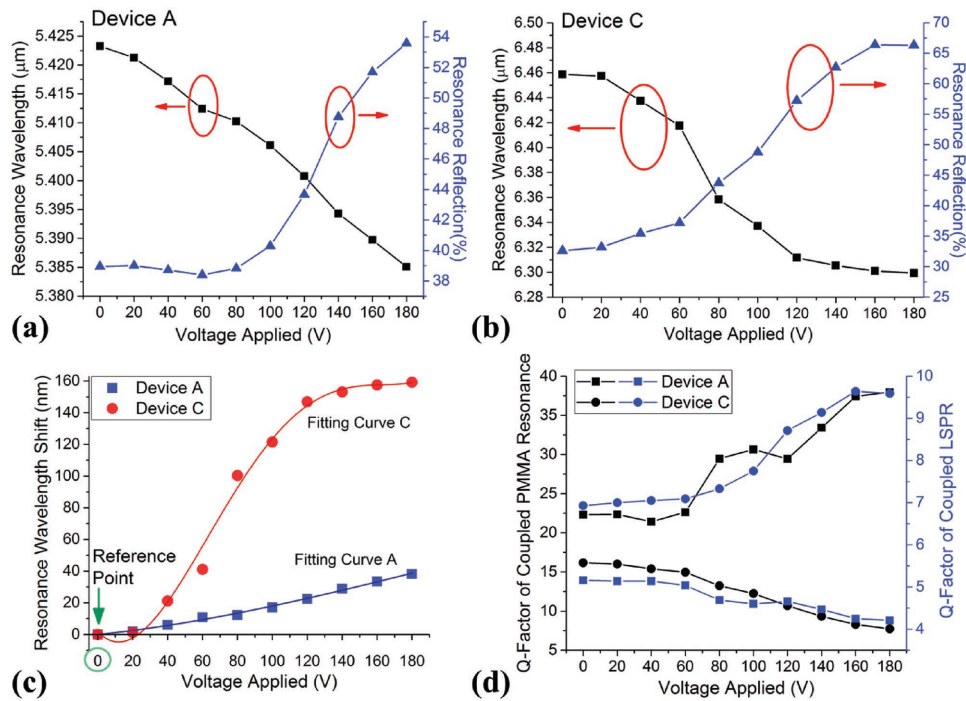


Figure 4. a) The measured LSPR wavelength and reflection intensity change versus the applied voltage of device A; b) The measured LSPR wavelength and reflection intensity change versus the applied voltage of device C; c) The measured LSPR wavelength shift as a function of the applied voltage of device A and C. The fitted data are conveyed by the solid line; d) The measured Q-factors of LSPR dip and Fano-like peak as a function of the applied voltage of device A and C through multipole fitting.

electromagnetic induced transparency (EIT) analogous resonance. The damping rate of PMMA is nearly constant from the fitted results, less than 0.446 THz. Imposed by the rising graphene doping level, the coupled LSPR's line shape becomes narrower and shifted to higher frequency except for device B which is reluctant to the electrical modulation. Likewise, the power of the coupling light $\Omega_C(\omega_c)$ is decreased for device A, increased for device C and leveled for device B. It is suspected that due to the nonnegligible error in curve fitting, the value $\Omega_C(\omega_c)$ of device B is between device A and device C. In total, the three-level model can satisfactorily reproduce and explain the coupling of phonon mode with plasmon polariton in the presence of graphene electrostatic tuning, especially

that device A and C are under substantial influence while device B is not.

2.4. Mode Splitting and Coupling Strength

Figure 6 shows the coupling process between resonances. Here we conduct the FDTD simulation by replacing the PMMA thin film with a dielectric medium with the similar refractive index but zero extinction to reconstruct the uncoupled LSPR. The uncoupled LSPR and phonon mode of three devices are separately delineated in Figure 6a,c,d and the coupled counterparts in Figure 6b,d,f. The strong

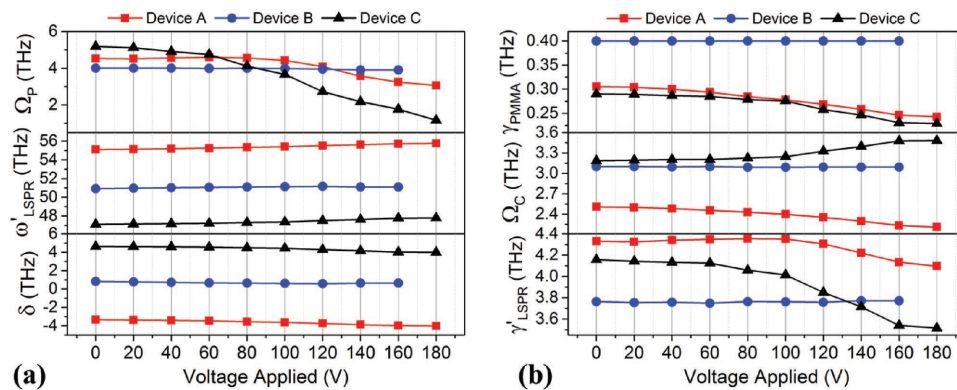


Figure 5. a) The extracted parameters Ω_p , ω_{LSPR} , and δ of three-level model for device A, B, and C at voltage applied from 0 to 180 V; b) The extracted parameters γ_{PMMA} , Ω_C , and γ_{LSPR} of three-level model for device A, B, and C at voltage applied from 0 to 180 V.

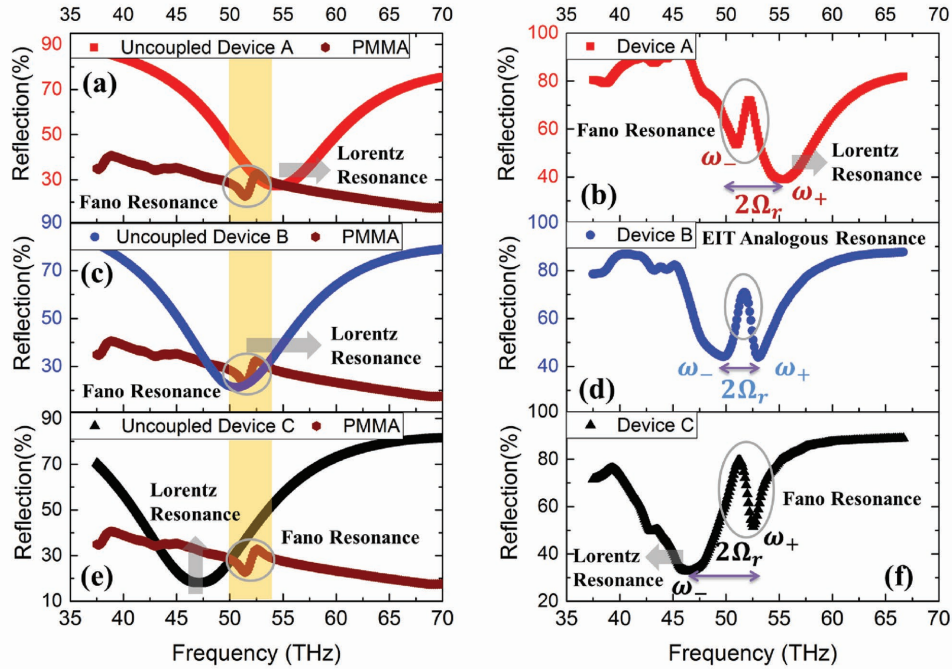


Figure 6. a) The uncoupled LSPR of device A and PMMA carbonyl resonance; b) The coupling of LSPR and PMMA carbonyl resonance leads to mode splitting in device A with the reinforced Fano and Lorentz resonance; c) The uncoupled LSPR of device B and the PMMA carbonyl resonance in vicinity; d) The coupling of LSPR and PMMA carbonyl resonance leads to mode splitting in device B with the EIT analogous resonance due to the highly overlapped uncoupled resonances; e) The uncoupled LSPR of device C and PMMA carbonyl resonance; f) The coupling of LSPR and PMMA carbonyl resonance leads to mode splitting in device C with the reinforced Fano and Lorentz resonance. The uncoupled LSPR spectra in a,c,e) are from FDTD simulation.

coupling of the two resonances in close proximity not only initiates the opening of the Fano-like reflection window but also engenders the split hybrid modes ω_- and ω_+ separated by split gap Ω_r in the form of energy transfer.^[11,13] Similar to vacuum-Rabi splitting, the coupled hybrid modes can be found through the energy state in the adiabatic Hamiltonian^[36,40,49,53]

$$H = \hbar \begin{bmatrix} \omega'_{\text{LSPR}} - j\frac{\gamma'_{\text{LSPR}}}{2}V & \\ V\omega_{\text{PMMA}} - j\frac{\gamma_{\text{PMMA}}}{2} & \end{bmatrix} \quad (8)$$

where V is the coupling strength. The eigen-frequencies ω_- and ω_+ can be calculated as

$$\omega_{\pm} = \frac{\omega'_{\text{LSPR}} + \omega_{\text{PMMA}}}{2} - \frac{j\gamma'_{\text{LSPR}} + j\gamma_{\text{PMMA}}}{4} \pm \sqrt{\left(\frac{\omega'_{\text{LSPR}} - \omega_{\text{PMMA}}}{2}\right)^2 + V^2 - \left(\frac{\gamma'_{\text{LSPR}} - \gamma_{\text{PMMA}}}{4}\right)^2 + \frac{(\omega'_{\text{LSPR}} - \omega_{\text{PMMA}})(j\gamma'_{\text{LSPR}} - j\gamma_{\text{PMMA}})}{4}} \quad (9)$$

Incorporating Equation (9) with $\Omega_r = \frac{\omega_+ - \omega_-}{2}$ (Ω_r is quantified as half of frequency difference of ω_- and ω_+ and $\hbar\Omega_r$ is the Rabi energy gap) the general expression of coupling strength is^[2]

$$V = \sqrt{\Omega_r^2 - \left(\frac{\omega'_{\text{LSPR}} - \omega_{\text{PMMA}}}{2}\right)^2 + \left(\frac{\gamma'_{\text{LSPR}} - \gamma_{\text{PMMA}}}{4}\right)^2} \quad (10)$$

When $\delta \approx 0$, a brief expression $V = \sqrt{\Omega_r^2 + \left(\frac{\gamma'_{\text{LSPR}} - \gamma_{\text{PMMA}}}{4}\right)^2}$ can be derived and applied to device B. Mode splitting condition $V > \left|\frac{\gamma'_{\text{LSPR}} - \gamma_{\text{PMMA}}}{4}\right|$ is satisfied in all the cases of this work.^[38]

Figure 7a is the anticrossing dispersion that describes the mode splitting of the coupled plasmon-phonon resonance.^[37] The data points are grouped into three parts due to the distinct splitting occasions for three devices and each subset contains a pile of hybrid states ω_{\pm} corresponding to the increased uncoupled LSPR frequencies in the sequence of 0–180 V. The inset is the magnified view of the coupled upper state ω_+ of device C, for instance, that the frequencies of the coupled hybrid states are increased with the applied voltage. The lower state of device C and upper state of device A are the coupled LSPRs which are under strong influence by graphene electrostatic modulation. However, the split modes of device B can hardly be influenced.

Subsequently, coupling strength V is investigated for all cases (Table 2). It is shown as a function of the uncoupled LSPR frequency in Figure 7b as well as the applied voltage in the inset.^[35] Device B possesses the largest coupling strength of around 8–8.1 meV (1.94–1.96 THz), to which the insensitivity to electrical tuning of the Fano-like resonance thus can be ascribed, i.e., the electrical pumping induced perturbation is not strong enough compared to the plasmon-phonon coupling strength. As opposed to device C, the coupling strength of device A is gradually reduced with the increased applied voltage. In other words, coupling strength decreases as the uncoupled LSPR mode departs from the carbonyl phonon mode.

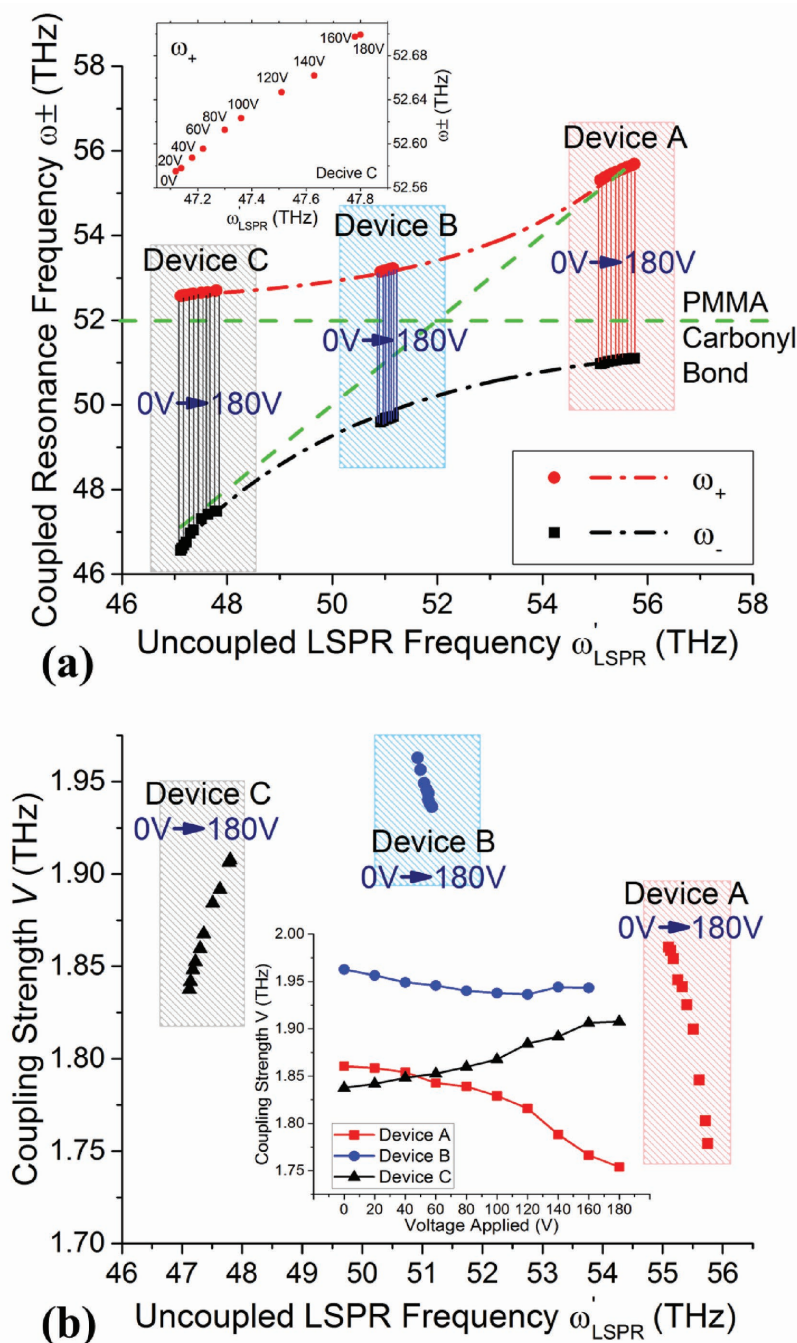


Figure 7. a) The frequency anticrossing dispersion of mode splitting occurred in the coupled LSPR and PMMA carbonyl resonance. The horizontal dash line indicates PMMA carbonyl resonance. The upper and lower hybrid states are scattered above and below this line. The diagonal dash line indicates the situation when the frequency of the coupled resonance is equal to that of the uncoupled LSPR. Inset: the zoomed-in example of the upper hybrid state of device C from 0 to 180 V; b) Coupling strength of three devices from 0 to 180 V as a function of the uncoupled LSPR frequency. Inset: The change of coupling strength of three devices as a function the applied voltage.

2.5. Possible Application: The Tunable and Dynamic Molecular Sensing Platform

The plasmonic sensing utilizing LSPR is reported to be ultrafast and fairly sensitive.^[54,55] Considering the scalability

and geometric diversity of metamaterial, ultrasensitive sensing is under continuous development by means of Fano resonance,^[7,56] nanocavity,^[57] etc. The dynamic sensing can be attributed to the electrical controllability of monolayer graphene in such hybrid platforms.^[1,58–60] **Figure 8a** conceptualizes molecular sensing on our proposed graphene-based tunable sensing platform on which the real-time, dynamic and label-free detection can be realized. The complementary metamaterial of the cross microvoid is able to generate the volumetric electric field enhancement and accordingly shows a characterization of sensitive detection when functionalized by molecule.

Figure 8b exhibits the distinctive reflection spectra of device C simulated under different background refractive indices (RI) ranging from 1.1 to 1.5 under various Fermi levels of monolayer graphene. LSPR is moved toward longer wavelength due to the increased refractive index of the sensing medium, while shifted to shorter wavelength due to the altered optical permittivity of the heavily doped monolayer graphene. The LSPR wavelength is reversely proportional to Fermi level for each case as shown in Figure S8 (Supporting Information). The detection range is extended by graphene electrostatic tuning. Figure 8c shows the linear redshift in LSPR wavelength with the sensing refractive index for each graphene Fermi level varying from 0.1 to 0.3 eV in a step of 0.05 eV. The slope of the refractive index dependence $\delta\lambda/\delta n$ (in $\mu\text{m RIU}^{-1}$) represents the sensitivity of RI plasmonic sensing. The inset table shows the sensitivity values of different doping cases, $1.677 \mu\text{m RIU}^{-1}$ in average which is not very much affected by the Fermi level of monolayer graphene. The refractive index induced redshift is replicated in the experiment for device C (**Figure 9a**) freshly fabricated on graphene monolayer. Here, we apply a large droplet of $100 \times 10^{-3} \text{ M}$ glucose solution in DI water onto the sample (not postthermal treated due to bonding process) and desiccate it to minimize the effect of water absorption during the measurement. The measured results show a LSPR wavelength shift of 120 nm. The observed wavelength shift indicates an increase of the effective refractive index of the surrounding by 7.2% due to the presence of the deposited glucose molecules.

Under the tuning-sensing condition of the $100 \times 10^{-3} \text{ M}$ glucose with the applied voltage varying from 0 to 80 V, the blueshift of LSPR wavelength is 40 nm, across from 6.509 μm to 6.470 μm , and the referenced LSPR of the nonglucose/bare device is at 6.387 μm in Figure 9b. For both this sensing case and the bare

Table 2. Coupling strength of device A, B, and C at different applied voltages.

| V [THz] | Device A | Device B | Device C |
|---------|----------|----------|----------|
| 0 V | 1.860 | 1.963 | 1.838 |
| 20 V | 1.859 | 1.957 | 1.842 |
| 40 V | 1.854 | 1.950 | 1.848 |
| 60 V | 1.843 | 1.946 | 1.853 |
| 80 V | 1.839 | 1.941 | 1.860 |
| 100 V | 1.829 | 1.938 | 1.868 |
| 120 V | 1.816 | 1.937 | 1.884 |
| 140 V | 1.788 | 1.945 | 1.892 |
| 160 V | 1.766 | 1.944 | 1.906 |
| 180 V | 1.754 | N.A. | 1.908 |

device whose LSPR wavelength shift of 40 nm can be reached at 60 V, the tuning effects are deviated from the ideal case of the linear correlation between LSPR wavelength shift and graphene

Fermi level through simulation. The main reason is due to the undesired postthermal treatment during bonding process.

Figure of merit (FoM) is defined as the ratio of sensitivity to FWHM (in μm), $\frac{\delta\lambda/\delta n}{\text{FWHM}}$, to quantify the resolution of LSPR sensors.^[5,61,62] In Figure 8d, FoM can be presented by both Fermi level and the sensing medium RI, with the maximum FoM highlighted for each RI. Fermi level at 0.25 eV ensures the best sensing resolution for the lower RI of 1 and 1.1 with the maximum FoMs of 1.042 and 0.899, respectively; the 0.2 eV Fermi level provides RI of 1.2 and 1.3 in the moderate range with the highest FoM values of 0.934 and 0.849; the optimum FoMs of 0.853 and 0.864 for higher RI of 1.4 and 1.5 is yielded by the Fermi level at 0.15 eV. This is suggested that the lower RI sensing can choose higher graphene doping level, while higher RI sensing medium should switch to lower graphene doping level to obtain the appreciable sensing resolution. Hence, the electrostatically tunable graphene-based metamaterial is demonstrated to be a promising hybrid plasmonic platform that can achieve dynamic sensing, broadened

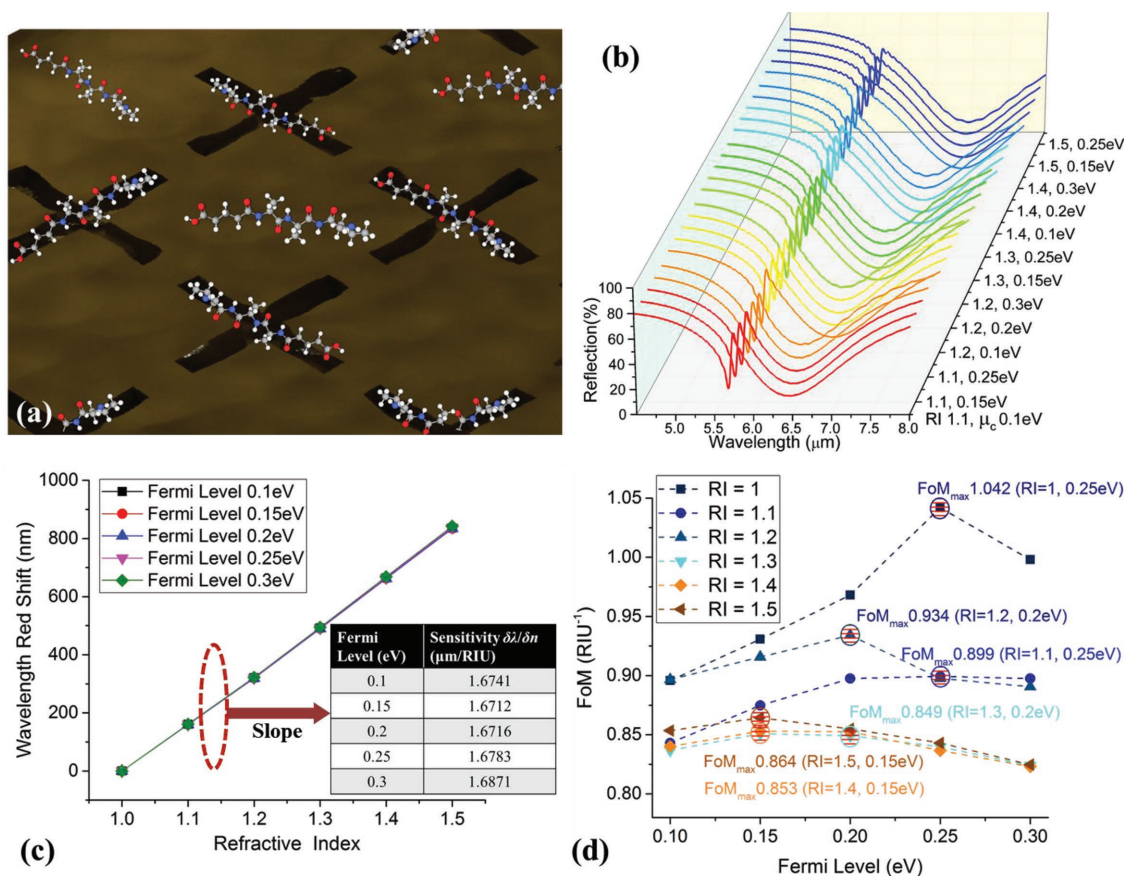


Figure 8. a) The schematic of the molecule-in-liquid sensing on the proposed graphene plasmonic hybrid sensing platform (device C); b) The simulated reflection spectra of the sensing medium of different refractive indices under the monolayer graphene modulation at different Fermi levels (device C); c) The simulated LSPR wavelength redshift at different Fermi levels versus the refractive index (device C). The slope of the wavelength shifts, or sensitivity at different Fermi levels are summarized in the inset table. d) Figure of merit of the sensing platform (device C) with different refractive index sensing medium at different graphene doping level. The maximum FoM for each refractive index is marked with the exact condition.

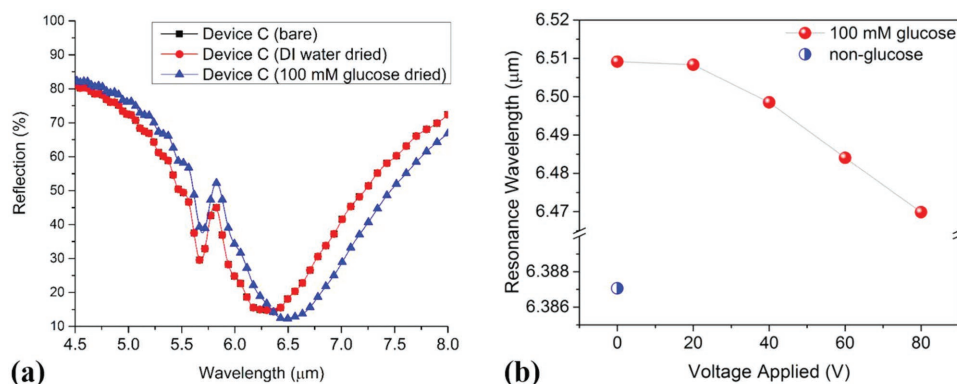


Figure 9. a) The experimentally observed sensing performance of device C. The effect of DI water treatment followed by the drying on the device characteristics is found to be negligible while the presence of glucose molecules on the surface induces strong wavelength shift of the structure; b) The experimentally demonstrated sensing-tuning effect of device C. With the glucose molecules applied on the surface of device C, the graphene electrostatic tuning effect is observed.

detection range and the controllable sensing resolution when in operation.

3. Conclusion

In summary, the electrically tunable graphene metamaterial resonator is presented in this work. Under graphene electrostatic modulation, significant variations such as wavelength shift, intensity and Q-factor change of the LSPR and Fano-like resonances are observed. The first reported experimental demonstration of the perfectly matched plasmon polariton–phonon case which is blind to graphene electrical modulation is intriguing. In numerical analysis, the parameters of the three-level model are extracted to manifest the modulating progress. The anticrossing feature of mode splitting during graphene electrostatic modulation is also delivered for the first time. It is shown that coupling strength is not only predominated by the device type but also affected by the graphene doping level, but with an exception for the matched coupling due to its maximum coupling strength. Finally, a possible application for the tunable multiplexed sensing is theoretically explained and experimentally demonstrated. The relationship observed between FoM and graphene doping level can be advantageous for real sensing environment where the targeting molecules are often delivered in various analyte conditions.

Supporting Information

Supporting Information is available from the Wiley Online Library or from the author.

Acknowledgements

The authors would like to thank Dr. Piotr Kropelnicki and Simon, Chun Kiat Goh from the School of Electrical and Electronic Engineering, Nanyang Technological University and Excelitas Technologies, Singapore for their kind support of chip bonding, and Jingxuan Wei for his kind help in the last fabrication. The authors acknowledge the financial support from the research grants of NRF-CRP15-2015-02 “Piezoelectric Photonics

Using CMOS Compatible AlN Technology for Enabling The Next Generation Photonics ICs and Nanosensors” (WBS: R-263000C24281) at NUS, Singapore; and the partial support by National Natural Science Foundation of China under Grant No. 61474078 at NUS (Suzhou) Research Institute, Suzhou, China.

Conflict of Interest

The authors declare no conflict of interest.

Keywords

Fano resonance, graphene tuning, mid-IR plasmonics, mode splitting, plasmon–phonon coupling

Received: January 11, 2018

Published online:

- [1] D. Rodrigo, O. Limaj, D. Janner, D. Etezadi, F. J. García de Abajo, V. Pruneri, H. Altug, *Science* **2015**, 349, 165.
- [2] K. Chen, R. Adato, H. Altug, *ACS Nano* **2012**, 6, 7998.
- [3] N. Liu, L. Langguth, T. Weiss, J. Kastel, M. Fleischhauer, T. Pfau, H. Giessen, *Nat. Mater.* **2009**, 8, 758.
- [4] B. Luk'yanchuk, N. I. Zheludev, S. A. Maier, N. J. Halas, P. Nordlander, H. Giessen, C. T. Chong, *Nat. Mater.* **2010**, 9, 707.
- [5] B. Gallinet, O. J. F. Martin, *ACS Nano* **2013**, 7, 6978.
- [6] Y. Yang, I. I. Kravchenko, D. P. Briggs, J. Valentine, *Nat. Commun.* **2014**, 5, 5753.
- [7] C. Wu, A. B. Khanikaev, R. Adato, N. Arju, A. A. Yanik, H. Altug, G. Shvets, *Nat. Mater.* **2011**, 11, 69.
- [8] C. Wu, N. Arju, G. Kelp, J. A. Fan, J. Dominguez, E. Gonzales, E. Tutuc, I. Brener, G. Shvets, *Nat. Commun.* **2014**, 5, 3892.
- [9] N. Dabidian, I. Kholmanov, A. B. Khanikaev, K. Tatar, S. Trendafilov, S. H. Mousavi, C. Magnuson, R. S. Ruoff, G. Shvets, *ACS Photonics* **2015**, 2, 216.
- [10] S. Hayashi, D. V. Nesterenko, A. Rahmouni, H. Ishitobi, Y. Inouye, S. Kawata, Z. Sekkat, *Sci. Rep.* **2016**, 6, 33144.
- [11] W. Wan, X. Yang, J. Gao, *Opt. Express* **2016**, 24, 12367.
- [12] J. P. Long, B. S. Simpkins, *ACS Photonics* **2015**, 2, 130.

- [13] D. J. Shelton, I. Brener, J. C. Ginn, M. B. Sinclair, D. W. Peters, K. R. Coffey, G. D. Boreman, *Nano Lett.* **2011**, *11*, 2104.
- [14] B. Lahiri, S. G. McMeekin, R. M. De la Rue, N. P. Johnson, *Opt. Express* **2013**, *21*, 9343.
- [15] G. Dayal, X. Y. Chin, C. Soci, R. Singh, *Adv. Opt. Mater.* **2017**, *5*, 1600559.
- [16] F. Cheng, X. Yang, J. Gao, *Sci. Rep.* **2015**, *5*, 14327.
- [17] Y. Cui, J. Zhou, V. A. Tamma, W. Park, *ACS Nano* **2012**, *6*, 2385.
- [18] W.-S. Chang, J. B. Lassiter, P. Swanglap, H. Sobhani, S. Khatua, P. Nordlander, N. J. Halas, S. Link, *Nano Lett.* **2012**, *12*, 4977.
- [19] W. M. Zhu, J. H. Teng, X. H. Zhang, J. M. Tsai, Q. Y. Wu, H. Tanoto, H. C. Guo, T. Bourouina, G. Q. Lo, D. L. Kwong, A. Q. Liu, presented at *25th Int. Conf. on Micro Electro Mechanical Systems (MEMS)*, IEEE, France, January **2012**.
- [20] M. Amin, M. Farhat, H. Bagci, *Sci. Rep.* **2013**, *3*, 2105.
- [21] M. Pan, Z. Liang, Y. Wang, Y. Chen, *Sci. Rep.* **2016**, *6*, 29984.
- [22] K. S. Novoselov, A. K. Geim, S. V. Morozov, D. Jiang, Y. Zhang, S. V. Dubonos, I. V. Grigorieva, A. A. Firsov, *Science* **2004**, *306*, 666.
- [23] Z. Q. Li, E. A. Henriksen, Z. Jiang, Z. Hao, M. C. Martin, P. Kim, H. L. Stormer, D. N. Basov, *Nat. Phys.* **2008**, *4*, 532.
- [24] T. Low, P. Avouris, *ACS Nano* **2014**, *8*, 1086.
- [25] A. Vakil, N. Engheta, *Science* **2011**, *332*, 1291.
- [26] E. S. Kulkarni, S. P. Heussler, A. V. Stier, I. Martin-Fernandez, H. Andersen, C.-T. Toh, B. Özyilmaz, *Adv. Opt. Mater.* **2015**, *3*, 34.
- [27] I. J. Luxmoore, P. Q. Liu, P. Li, J. Faist, G. R. Nash, *ACS Photonics* **2016**, *3*, 936.
- [28] G. X. Ni, L. Wang, M. D. Goldflam, M. Wagner, Z. Fei, A. S. McLeod, M. K. Liu, F. Keilmann, B. Özyilmaz, A. H. Castro Neto, J. Hone, M. M. Fogler, D. N. Basov, *Nat. Photonics* **2016**, *10*, 244.
- [29] V. W. Brar, M. S. Jang, M. Sherratt, J. J. Lopez, H. A. Atwater, *Nano Lett.* **2013**, *13*, 2541.
- [30] U. Sassi, R. Parret, S. Nanot, M. Bruna, S. Borini, D. De Fazio, Z. Zhao, E. Lidorikis, F. H. Koppens, A. C. Ferrari, A. Colli, *Nat. Commun.* **2017**, *8*, 14311.
- [31] Y. Li, H. Yan, D. B. Farmer, X. Meng, W. Zhu, R. M. Osgood, T. F. Heinz, P. Avouris, *Nano Lett.* **2014**, *14*, 1573.
- [32] N. K. Emani, T. F. Chung, X. Ni, A. V. Kildishev, Y. P. Chen, A. Boltasseva, *Nano Lett.* **2012**, *12*, 5202.
- [33] S. Kim, M. S. Jang, V. W. Brar, Y. Tolstova, K. W. Mauser, H. A. Atwater, *Nat. Commun.* **2016**, *7*, 12323.
- [34] N. K. Emani, T.-F. Chung, A. V. Kildishev, V. M. Shalaev, Y. P. Chen, A. Boltasseva, *Nano Lett.* **2014**, *14*, 78.
- [35] G. A. Wurtz, P. R. Evans, W. Hendren, R. Atkinson, W. Dickson, R. J. Pollard, A. V. Zayats, W. Harrison, C. Bower, *Nano Lett.* **2007**, *7*, 1297.
- [36] S. Savasta, R. Saija, A. Ridolfo, O. Di Stefano, P. Denti, F. Borghese, *ACS Nano* **2010**, *4*, 6369.
- [37] A. E. Schlather, N. Large, A. S. Urban, P. Nordlander, N. J. Halas, *Nano Lett.* **2013**, *13*, 3281.
- [38] K. Santhosh, O. Bitton, L. Chuntonov, G. Haran, *Nat. Commun.* **2016**, *7*, ncomms11823.
- [39] H. Chen, L. Shao, K. C. Woo, J. Wang, H.-Q. Lin, *J. Phys. Chem. C* **2012**, *116*, 14088.
- [40] A. A. Kazemi, B. C. Kress, E. A. Mendoza, M. F. Finch, B. A. Lail, *Proc. SPIE* **2014**, *9202*, 92021B.
- [41] F. Falcone, T. Lopetegui, M. A. G. Laso, J. D. Baena, J. Bonache, M. Beruete, R. Marqués, F. Martín, M. Sorolla, *Phys. Rev. Lett.* **2004**, *93*, 197401.
- [42] T. Zentgraf, T. P. Meyrath, A. Seidel, S. Kaiser, H. Giessen, C. Rockstuhl, F. Lederer, *Phys. Rev. B* **2007**, *76*, 033407.
- [43] D. Hasan, C. P. Ho, P. Pitchappa, B. Yang, C. Yang, C. Lee, *Sci. Rep.* **2016**, *6*, 22227.
- [44] S. Cakmakyapan, H. Caglayan, E. Ozbay, *Carbon* **2014**, *80*, 351.
- [45] B. Huard, J. A. Sulpizio, N. Stander, K. Todd, B. Yang, D. Goldhaber-Gordon, *Phys. Rev. Lett.* **2007**, *98*, 236803.
- [46] Y. Sun, W. Tan, L. Liang, H. T. Jiang, Z. G. Wang, F. Q. Liu, H. Chen, *Europhys. Lett.* **2012**, *98*, 64007.
- [47] N. Xu, M. Manjappa, R. Singh, W. Zhang, *Adv. Opt. Mater.* **2016**, *4*, 1179.
- [48] T. Weiss, M. Mesch, M. Schaferling, H. Giessen, W. Langbein, E. A. Muljarov, *Phys. Rev. Lett.* **2016**, *116*, 237401.
- [49] A. Salomon, R. J. Gordon, Y. Prior, T. Seideman, M. Sukharev, *Phys. Rev. Lett.* **2012**, *109*, 073002.
- [50] Y. K. Srivastava, M. Manjappa, L. Cong, W. Cao, I. Al-Naib, W. Zhang, R. Singh, *Adv. Opt. Mater.* **2016**, *4*, 457.
- [51] W. Wan, W. Zheng, Y. Chen, Z. Liu, *Nanoscale* **2014**, *6*, 9093.
- [52] S. Zhang, D. A. Genov, Y. Wang, M. Liu, X. Zhang, *J. Phys. Rev. Lett.* **2008**, *101*, 047401.
- [53] A. D. Boardman, D. P. Tsai, M. F. Finch, B. A. Lail, *Proc. SPIE* **2015**, *9547*, 954710.
- [54] J. N. Anker, W. P. Hall, O. Lyandres, N. C. Shah, J. Zhao, R. P. Van Duyne, *Nat. Mater.* **2008**, *7*, 442.
- [55] R. Adato, H. Altug, *Nat. Commun.* **2013**, *4*, 2154.
- [56] F. López-Tejiera, R. Paniagua-Domínguez, J. A. Sánchez-Gil, *ACS Nano* **2012**, *6*, 8989.
- [57] N. Verellen, P. Van Dorpe, C. Huang, K. Lodewijks, G. A. Vandenbosch, L. Lagae, V. V. Moshchalkov, *Nano Lett.* **2011**, *11*, 391.
- [58] W. Tang, L. Wang, X. Chen, C. Liu, A. Yu, W. Lu, *Nanoscale* **2016**, *8*, 15196.
- [59] H. Hu, X. Yang, F. Zhai, D. Hu, R. Liu, K. Liu, Z. Sun, Q. Dai, *Nat. Commun.* **2016**, *7*, 12334.
- [60] J. C. Reed, H. Zhu, A. Y. Zhu, C. Li, E. Cubukcu, *Nano Lett.* **2012**, *12*, 4090.
- [61] K. L. Lee, C. C. Chang, M. L. You, M. Y. Pan, P. K. Wei, *Sci. Rep.* **2016**, *6*, 33126.
- [62] N. Liu, M. Mesch, T. Weiss, M. Hentschel, H. Giessen, *Nano Lett.* **2010**, *10*, 2342.